ADVANCED MATERIALS
www.advmat.de

Kirigami-Inspired Pressure Sensors for Wearable Dynamic Cardiovascular Monitoring

Keyu Meng, Xiao Xiao, Zixiao Liu, Sophia Shen, Trinny Tat, Zihan Wang, Chengyue Lu, Wenbo Ding, Ximin He, Jun Yang, and Jun Chen**

Continuously and accurately monitoring pulse-wave signals is critical to prevent and diagnose cardiovascular diseases. However, existing wearable pulse sensors are vulnerable to motion artifacts due to the lack of proper adhesion and conformal interface with human skin during body movement. Here, a highly sensitive and conformal pressure sensor inspired by the kirigami structure is developed to measure the human pulse wave on different body artery sites under various prestressing pressure conditions and even with body movement. COMSOL multiphysical field coupling simulation and experimental testing are used to verify the unique advantages of the kirigami structure. The device shows a superior sensitivity (35.2 mV Pa^{-1}) and remarkable stability (>84 000 cycles). Toward practical applications, a wireless cardiovascular monitoring system is developed for wirelessly transmitting the pulse signals to a mobile phone in real-time, which successfully distinguished the pulse waveforms from different participants. The pulse waveforms measured by the kirigami inspired pressure sensor are as accurate as those provided by the commercial medical device. Given the compelling features, the sensor provides an ascendant way for wearable electronics to overcome motion artifacts when monitoring pulse signals, thus representing a solid advancement toward personalized healthcare in the era of the Internet of Things.

1. Introduction

Cardiovascular diseases (CVDs) lead to more than 18 million deaths each year and are the top cause of death worldwide.[1,2] The human pulse wave, as one of the most representative vital signs, has historically been a significant source of physiological information for clinical health evaluation.[3,4] The variations in pulse waveforms are also important basis assessments of human cardiovascular system (blood flow, peripheral resistance, and vascular elasticity), which are related to the CVDs, such as arteriosclerosis, myocardial infarction, and hypertension.[5–8] Real-time accurate pulse waveform measurements have a crucial effect for pulse-based health monitoring and diagnosis of CVDs. The current rapid advancement of wearable technologies allows them to provide real-time and continuous pulse wave monitoring,[9,10] based on capacitive,[11–15] piezoresistive,[16–19] piezoelectric,[20–22] triboelectric,[23–27] magnetoelastic,[28–30] photoplethysmography (PPG),[31–34] and ultrasonic.[35–38] However, these wearable sensors are generally vulnerable to body motion artifacts, leading to inaccurate diagnosis and misinterpretation,[39–42] which are mainly ascribed to the weak adhesion or poor conformability, and thus inconsistent interfaces between the devices and human skin. To eliminate motion artifacts, most efforts are dedicated to signal processing, machine learning, and artificial intelligence.[43] However, the complex data analysis involved in the software development process complicates wearable bioelectronics. Meanwhile, high power consumption computing chips will significantly increase their production costs. Although motion artifact removal techniques have obtained many achievements, the motion artifacts in pulse waveform measurement remain a challenge since mechanical

K. Meng
School of Electronic and Information Engineering
Jilin Provincial Key Laboratory of Human Health Status Identification and Function Enhancement
Changchun University
Changchun 130022, China

K. Meng, X. Xiao, S. Shen, T. Tat, J. Chen
Department of Bioengineering
University of California, Los Angeles
Los Angeles, CA 90095, USA
E-mail: jun.chen@ucla.edu

The ORCID identification number(s) for the author(s) of this article can be found under https://doi.org/10.1002/adma.202202478.

Z. Liu, X. He
Department of Materials Science and Engineering
University of California, Los Angeles
Los Angeles, CA 90095, USA

Z. Wang, C. Lu, W. Ding
Tsinghua-Berkeley Shenzhen Institute and Tsinghua Shenzhen International Graduate School
Tsinghua University
Shenzhen 518055, P. R. China

J. Yang
Chongqing Institute of Green and Intelligent Technology
Chinese Academy of Sciences
Chongqing 400714, P. R. China
E-mail: jyang@cigit.ac.cn

DOI: 10.1002/adma.202202478

disturbances appear at the interface of human skin tissue.[44] Specifically, highly deformation and distortion of the human arterial vessel under large static force are the primary sources of motion artifacts.

Kirigami construction has been credited with developing stretchable devices by using cutting patterns in polymer substrates with a laser beam or direct-printing process.[45,46] As kirigami structure generates geometric deformations that govern the inherent elasticity of the material, the characteristics of kirigami are affected by the pattern and orientation of these cuts. For kirigami-structured sensors, most of the reported applications are operated in the horizontal direction and demonstrate a highly controllable stretchability.[47–50] Fewer explorations are taking advantage of the unique stretching properties of papercut structures in the vertical direction. By changing the geometry of the 3D kirigami structure, such as the number of cuts and the size of the cuts in the pattern, it is possible to make the device highly stretchable and conformable. These characteristics of kirigami make it ideal for developing stretchable and wearable sensors to reduce the interference caused by motion artifacts.

Herein, we first demonstrate a highly conformal and cost-effective kirigami-inspired pressure (KIP) sensor for wireless cardiovascular monitoring. Since the pulse wave is in the vertical direction, we exploit the 3D vertical kirigami-inspired notches to adjust the deformability of our device to enhance conformability and breathability. Specifically, when an external pressure is applied to the sensor, gaps could be squeezed out of the inlet of the kirigami-shaped layer, resulting in large elastic deformation. This provides ample space for the two triboelectric layers to move relationally and allows for a full contact-separation. To verify that the structure has the above advantages, we used the Solid Mechanics module in COMSOL multiphysics to simulate the structural contact of the triboelectric layers to obtain a more quantitative understanding of this electricity generation process. Furthermore, nanowire pattern was modified on the surface of the triboelectric materials that could improve the force distribution and allow sufficient elastic deformation under prestressing pressures. Such multilevel structure endows the KIP sensor with preeminent properties, including a particular sensitivity of up to 35.2 mV Pa^{-1}, a wide frequency response range (≈15 Hz), and dramatic stability after >84 000 operation cycles. Furthermore, a wireless cardiovascular monitoring system was developed based on the KIP sensor for personalized health data acquisition, real-time wireless data transmission, and display on a mobile phone graphical user interface (GUI). The system can perform long-time continuous pulse wave monitoring, as well as identifying people of different ages and health conditions via the differences in the waveforms. Compared to commercially available clinical-level monitors, the characteristic points of the pulse waves measured by the KIP sensor are consistent with that measured by the photoelectric sensor probe. Based on the compelling features of our device, no additional hardware or computation is required to avoid motion artifacts for capturing pulse waveforms from different body parts, including fingertip, brachial artery, which provide an unprecedented approach to a long-standing challenge in wearable electronics, and customizability personalized cardiovascular care.

2. Results and Discussions

2.1. Design and Fabrication of the Kirigami-Inspired Pressure Sensor

The kirigami structural representation of the basic KIP sensor is shown in **Figure 1**a. Two of the most effective methods for improving triboelectric output are selecting appropriate triboelectric materials and surface morphology treatment. Owing to their suitable mechanical properties, poly(tetrafluoroethylene) (PTFE) and poly(ethylene terephthalate) (PET) were chosen as the triboelectric layers and indium tin oxide (ITO) as the electrode. The PET and PTFE layers are combined by optical clear adhesive (OCA) adhered to the four corners of the device. We chose 50 μm thickness of OCA for the experiment since it is easier to be processed. When the external pressure is applied, the PET and PTFE layers are brought into contact with each other. The external pressure induced periodic contact and separation will generate electrical signals for sensing. To enhance the sensitivity and surface charge density on the PTFE surface, we fabricated a vertical kirigami structure and created nanowires via plasma etching and laser cutting (Figure 1b). The scanning electron microscopy (SEM) images of PTFE nanowires, which improved surface roughness, under different magnifications, are presented in Figure 1c and Figure S1, Supporting Information. The nanowires have the advantage of not only enhancing the surface triboelectrification and inducing a larger triboelectric charge density for higher electrical output, but also can be easily deformed under external subtle mechanical excitation for higher sensitivity. The detailed device fabrication process is presented in the Section 4 and Figure S2, Supporting Information. Figure 1d illustrates the as-fabricated flexible KIP sensor with dimensions of $2.6 \times 1.4 \times 0.0012$ cm^3, which can provide excellent flexibility (Figure S3, Supporting Information).

As a result of its distinct structure and material properties, the KIP sensor is lightweight, thin, and even transparent, allowing for a wide range of applications. Furthermore, the significant enhancement in elastic deformation capacity and adaptability to different external prestressing pressures due to the vertical kirigami structure ensures that the KIP sensor can be conformally attached to the human skin, which can be utilized for accurate pulse waveform monitoring, as presented in Figure 1e. Based on the KIP sensor, a wireless cardiovascular monitoring system was developed (Figure 1f), comprising of a KIP sensor to acquire the raw pulse wave signal, an analog conditioning circuit, an analog-to-digital converter, and a Bluetooth module to transmit the processed pulse signal to a mobile phone.

2.2. COMSOL Simulation

The working principle of the KIP sensor for pulse wave measurement can be described by its mechanical and electrical properties as follows: pulse pressure induces membrane deformation and the subsequent membrane vibration results in electric signal output.[51–55] The schematical illustration of the kirigami structure is presented in **Figure 2**a, where the length

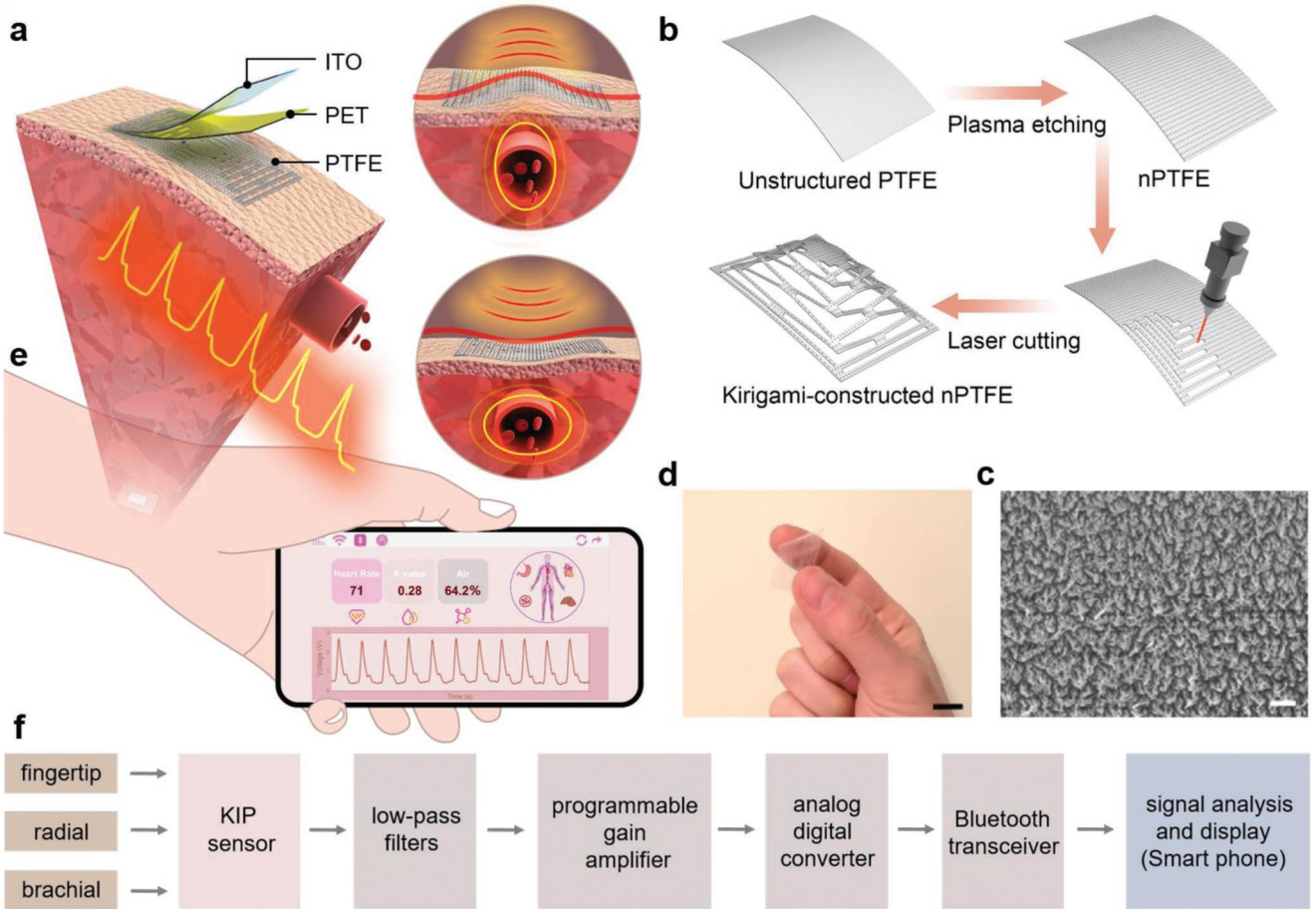

Figure 1. Design and fabrication of a KIP sensor. a) Schematic illustration of the as-fabricated KIP sensor containing a three-layer configuration: PTFE film and PET substrate as the two electrification layers, with a third layer of ITO coated onto the surface of PET acting as electrode. b) Schematic illustration showing the fabrication procedure for kirigami constructed nanowire PTFE (nPTFE). c) SEM images of nanowire-patterned PTFE (Scale bar: 1 µm). d) Photograph of the as-fabricated KIP sensor, demonstrating its excellent flexibility (Scale bar: 1 cm). e) A KIP sensor-based wireless cardiovascular monitoring system performs continuous pulse wave monitoring, and cardiovascular parameters are simultaneously displayed on a mobile phone via wireless transmission. f) Schematic diagram of the KIP sensor based wireless cardiovascular monitoring system.

(*a*) is 1.4 cm, the width (*b*) is 2.6 cm, the stripe (*d*) is 0.5 mm, and the seam spacing (*h*) is 0.3 mm. To qualitatively understand the electron transfer process, Figure 2b illustrates the potential energy profile of two atoms, one of PTFE and one of PET, during the charge transfer process. Before contact, the electrons cannot transfer due to the local trapping effect of the potential wells. When the ventricles contract, the generated blood pressure drives the movement of the PTFE membrane to become in contact with PET. As a result, the initial single potential well becomes an asymmetric double-well potential, where the electron can now hop from the PET atom to the PTFE atom. During diastole, when the ventricles expand, the two materials will begin to separate, but most of the electrons transferred to PTFE will be kept. Thus, contact-electrification occurs with the positively charged PET and negatively charged PTFE.

To obtain a more quantitative understanding of this electricity generation process, the KIP sensor was modeled as a capacitor in COMSOL Multiphysics, wherein an air gap is sandwiched between the PTFE and PET films. Solid Mechanics module was used to simulate the structural contact of the triboelectrics layers, which generates electricity and induces the variation of open-circuit voltage V_{oc}. The external pressure can deform the PTFE film and change the thickness of the air gap. The separation of PTFE and PET generates an electric potential difference. In an open-circuit configuration, the V_{oc} variation is proportional to the variation of the air-gap thickness *t*, which can be estimated by

$$V_{oc}(x) = \frac{\sigma t(x)}{\varepsilon_0} \tag{1}$$

where σ is the triboelectric surface charge density, and ε_0 is the vacuum permittivity. Vectors related to the spatial position are denoted in bold. The electric potential on the PET film is specified to be zero. In COMSOL, due to the geometric symmetry of the KIP sensor, only a single quadrant of the geometry needs to be modeled. Floating potential boundary conditions (charge $Q_0 = 0$) are applied to the top surface of PTFE and the bottom surface of PET to simulate the open-circuit condition.

As schematically illustrated in Figure 2c,g, we compare the KIP sensor with different structural designs, including PTFE with kirigami structure and PTFE without kirigami structure, to verify the advantages of kirigami structures in device output

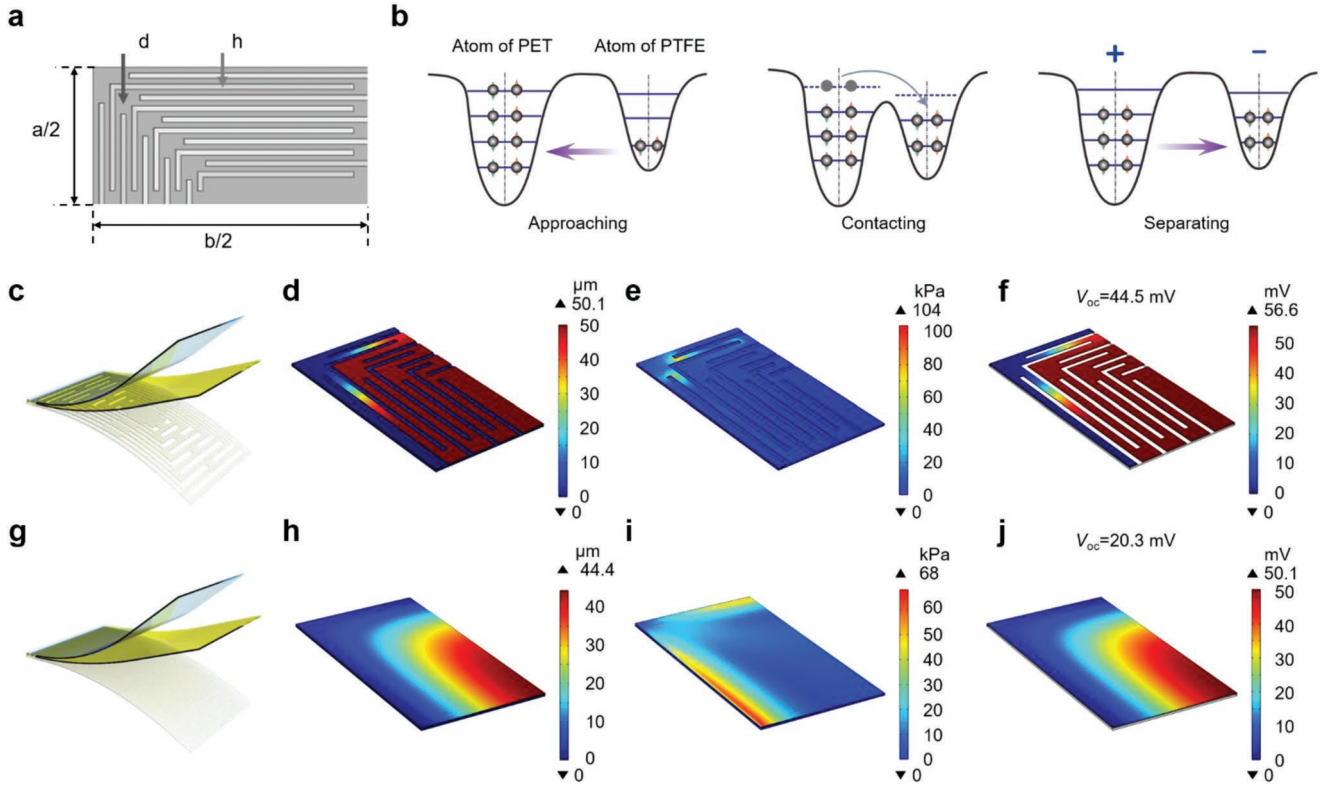

Figure 2. COMSOL simulation for the variation of V_{oc} with external load. a) Dimensions of the kirigami structure. b) Schematic of the potential energy profile of two atoms belonging to PTFE and PET, when they are before contact, in contact, and after contact. c,g) Schematic illustration of PTFE with kirigami structure (c) and PTFE without kirigami structure (g). COMSOL simulations for pressure sensors under 1 Pa pressure. d–f) Distributions of displacement (d), stress (e), and electric potential (f) of the kirigami-constructed sensor with ratio of 0.5/0.3 mm. h–j) Distributions of displacement (h), stress (i), and electric potential (j) of the sensor without kirigami structure. Due to the geometric symmetry of the sensor, only a single quadrant of the geometry was modeled. The electric potential on the PET film is specified to be zero.

performances. Initially, the triboelectric layers are separated by a 50-μm spacer. Then, a 1 Pa external pressure is exerted on the PTFE films with and without kirigami structure, respectively, to demonstrate the superior sensitivity of kirigami structure. Since the kirigami structure effectively removes geometric constraints from the film and introduces more degrees of freedom, it produces greater deformation at a given load, as shown in Figure 2. The kirigami-constructed PTFE (d/h = 0.5/0.3 mm, Figure 2d) can produce an average displacement of 39.4 μm at 1 Pa, while the PTFE without kirigami can only generate an average displacement of 18.0 μm (Figure 2h). The electric potential distributions of the sensors subjected to the external loads have been shown in Figure 2f,j. The average V_{oc} produced by the kirigami-constructed sensor is 44.5 mV, while the sensor without kirigami structure can only generate an average V_{oc} of 20.3 mV. Thus, under a load of 1 Pa, the kirigami structure can improve the sensitivity of the sensor by 2.2 times. The stress distributions of the sensors with and without the kirigami structure are shown in Figure 2e,i.

Furthermore, the kirigami-constructed sensors with different d/h ratios of 0.5/0.3, 0.5/0.5, and 0.5/0.7 mm for the stripe to seam spacing were modeled in COMSOL Multiphysics. An external pressure of 1 Pa is imposed on these sensors to investigate the effect of geometric design on the output signal. The deformation and stress distribution of the sensors are shown in Figures S4a,d,g and S4b,e,h, Supporting Information respectively. As the d/h ratio decreases from 0.5/0.3 to 0.5/0.7 mm, the kirigami-constructed PTFE film deforms less. Therefore, according to the proportional relationship in Equation (1), sensors with larger deformation can produce larger V_{oc}. The electric potential distributions of the sensors subjected to a 1 Pa external load are shown in Figure S4c,f,i. The average V_{oc} produced by the sensors with the ratios of 0.5/0.3, 0.5/0.5, and 0.5/0.7 mm is 44.5, 41.2, and 38.6 mV, respectively. Therefore, the geometric design of the kirigami pattern greatly affects the device sensitivity. A larger ratio of the stripe (d) to seam spacing (h) can lead to a larger deformation and a higher sensitivity.

2.3. Performance Evaluation

To quantitatively characterize properties of the KIP sensor, a customized measuring system utilizing a high precision force gauge and an electrodynamic shaker was employed to provide a precisely controlled periodic load as the input stimuli (Figure S5, Supporting Information). **Figure 3**a presents the influence of the three different structures on the output voltage. Under the constant pressure of 0.27 kPa at a frequency of 1 Hz, patterning PTFE triboelectric layer with a kirigami structure has been shown to improve sensitivity by over 4.9 times

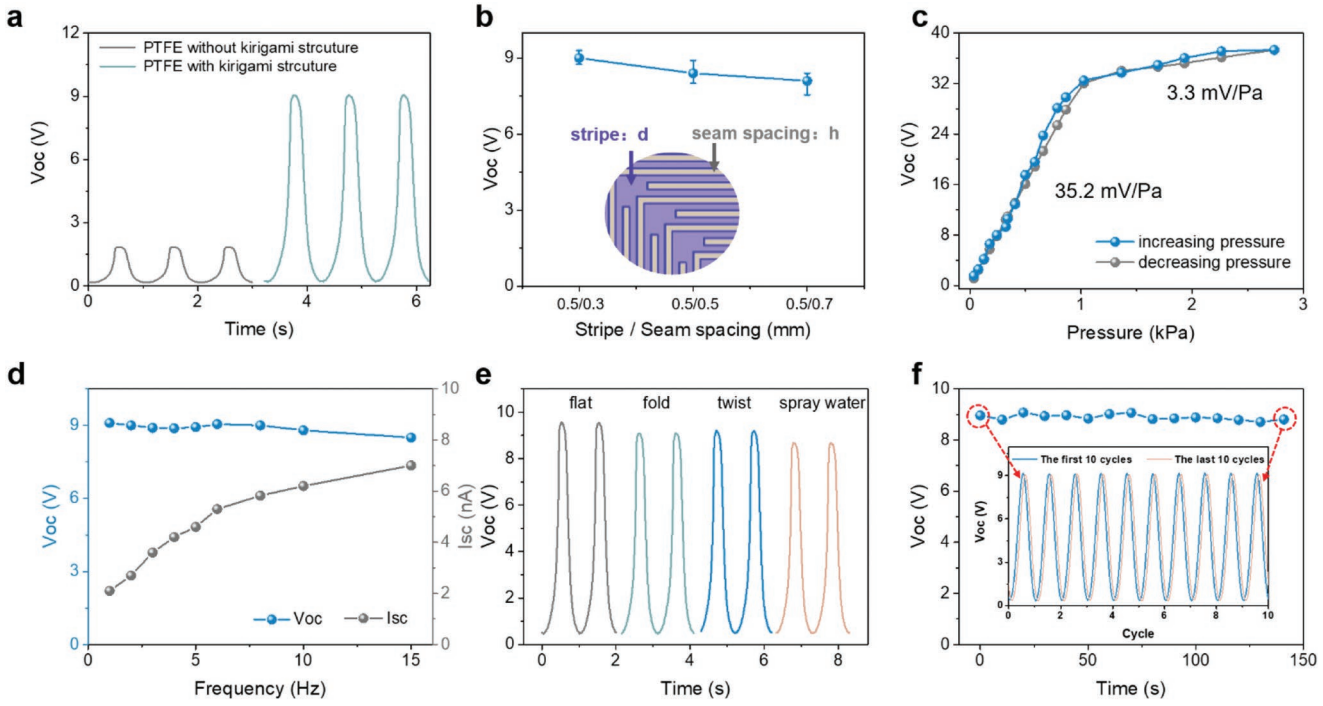

Figure 3. Electrical characteristic of the KIP sensor. a) Influence of the different sensor structure designs on the output voltage. b) Impact of the ratio of the stripe to seam spacing on the output performance of the KIP sensor. c) Open-circuit voltage of the KIP sensor under various applied pressures. d) V_{oc} and I_{sc} change of the KIP sensor under constantly applied pressure with frequencies from 1–15 Hz. e) Voltage changes of the KIP sensor after suffering various extreme conditions involving 200 cycles of folding, twisting, and being sprayed with water. f) Real-time V_{oc} of the KIP sensor for more than 84 000 loading/unloading cycles. There is no observable performance degradation.

compared to PTFE without kirigami structure layers of equivalent dimensions. This is because PTFE with kirigami structure will compress more for a given applied pressure, resulting in higher mechanical deformations and consequently higher output voltage. Admittedly, there is a discrepancy in the sensitivity enhancement between the simulation (2.2 times) and experimental results (4.9 times). This may be caused by a non-ideal test environment. Ambient humidity and temperature may affect the structural deformation and electrical properties of the sensor. Humidity transport and heat transfer can generate additional inelastic strains (hygroscopic strains ε_{hs} and thermal strain ε_{th}) in the polymer films and produce greater deformations. In addition, the environmental humidity and temperature also show an impact on the dielectric constant and resistance of the KIP sensors.

Additionally, the aforementioned ratio of the stripe to seam spacing of the kirigami structure also impacts the output performance. To study this, we fabricated the KIP sensors with the same three ratio conditions as previously mentioned (0.5/0.3, 0.5/0.5, 0.5/0.7 mm), and their images are shown in Figure S6, Supporting Information. Each of the three devices was evaluated under the same external pressure; the KIP sensor with a seam spacing of 0.3 mm delivered the highest output voltage and thus, best sensing performance (Figure 3b). Using this optimal stripe to seam spacing ratio of 0.5/0.3 mm ensures contact between the PTFE and PET layers under a certain external pressure level, allowing for charge replenishment and making the device more sensitive.

Optimizing the kirigami inspired pressure sensor to provide the highest possible sensitivity is crucial for accurate practical operation. To validate the performance of the previously optimized design, we performed multiple loading-unloading measurements to investigate the relationship between the applied external pressure and electrical output at a constant frequency of 1 Hz (Figure 3c and Figure S7, Supporting Information). The open-circuit voltage and short-circuit current show two distinct sensitivities under different pressure regions. There was a well-behaved linear variation in the low-pressure region of under 1 kPa in both the output voltage and current, with a superior sensitivity of 35.2 mV Pa^{-1} and 15.6 nA kPa^{-1}, respectively. In the high-pressure region (>1 kPa), a lower voltage sensitivity of 3.3 mV Pa^{-1} and a current sensitivity of 1.6 nA kPa^{-1} were experimentally observed due to the saturation of the effective contact-separation area.

The frequency response characteristics for the KIP sensor are shown in Figure 3d, which demonstrates the dependence of voltage and current amplitude under the constant pressure on various frequencies. An increase in the frequency loading from 1 to 15 Hz results in almost no change in the open-circuit voltage, but an increase in the amplitude of the short-circuit current is observed. The detailed information in Figure S8, Supporting Information demonstrates that the KIP sensor is capable of operating effectively under frequencies of 2, 4, 6, and 8 Hz, all of which well satisfy the requirements necessary for physiological monitoring, where the main frequency component is typically ≈10 Hz.

As the KIP sensor is intended to be a skin-compatible device, it is also necessary to be bendable and conformable to human skin. When tested under different curvatures (5 cm, 3 cm, 1 cm), the KIP sensor showed no performance discrepancy in output voltage (Figure S9, Supporting Information), demonstrating that it is thin enough to be bent and appropriately respond to external pressure when attached to various curved surfaces. Owing to its material and structural flexibility, the KIP sensor holds excellent softness and the capacity of withstanding bending under 180° and twisting under 360° after 200 cycles (Figure S10, Supporting Information), and even with water spraying (Figure S11, Supporting Information), as presented in Figure 3e. Additionally, the mechanical stability of the KIP sensor is also an important characteristic when used in human pulse monitoring, especially involving continuous and long-term use. After the KIP sensor was continuously tested under a pressure of 0.27 kPa for 84 000 loading/unloading cycles, there is a negligible output voltage discrepancy, which demonstrates the remarkable repeatability and durability of the KIP sensor. The output voltages of the first and the last ten cycles are depicted in Figure 3f. The above tests show that the KIP sensor can maintain admirable sensing performance under various extreme conditions for a long time.

2.4. Pulse Monitoring under Different Prestressing Pressures

To accurately and continuously monitor arterial pulse waves in daily life, the sensor must maintain high sensitivity and stability under a wide range of prestressing pressures in order to discriminate the subtle blood pressure change. To investigate the KIP sensor's performance, we applied five different prestressing pressures (1.3–18.6 kPa) on the fingertip, radial artery, and brachial artery by gently attaching the KIP sensor and wrapping the limb parts with a blood pressure gauge. Since the optimal inflation level is different based on the limb part, the radial arterial prestressing pressure range is different from the finger and brachial artery. During the experiment, we choose the blood pressure cuff with the most suitable size according to the different body parts (Figure S12, Supporting Information). For example, we chose the blood pressure cuff with the smallest length (6–11 cm) when measuring the pulse signal of fingertip, otherwise, the maximum inflation level during pressurization is not enough to make the finger feel the pressure, which is meaningless for measuring the pulse signal of the finger under different prestressing pressures. As for participant's wrist, we chose the blood pressure cuff with a length of 10–19 cm. When the applied pressure increases to 7.8 kPa, it is difficult to be pressurized and expanded. **Figure 4**a–c shows how the KIP sensor was directly attached to the fingertip (Movie S1, Supporting Information), radial artery (Movie S2, Supporting Information), and brachial artery. The real-time pulse wave data from the differing prestressing pressures, which were measured for more than 10 s, were transmitted online and displayed on a mobile phone APP. The resulting pulse waveforms are shown in Figure 4d–f, where there is a slight drop in amplitude as the pressure increases up to 13.3 kPa due to over-compression of the blood vessels and a rapid decrease at 18.6 kPa. These results agree well with the previous studies and existing literature on pulse wave monitoring.[9,56]

Furthermore, we quantitively analyzed the consistency of waveforms of these three human limb parts under the different prestressing pressures, and the normalized waveforms were shown in Figure 4g–i. The pressures on the x and y axis are both prestressing pressures. The pulse waveforms under different prestressing pressures were first normalized, and then analyzed with their correlation coefficient (R). The reported R-values were calculated for groups using the Origin software and correlation coefficients. The detailed analyzed results are shown in Figure S13, Supporting Information. It can be seen that the correlation coefficient between any two sets of waveforms under the constant pressure of the same limb part is greater than 0.88. Additionally, no noticeable distortion is observed, and the contour of the waveform remains highly consistent, indicating a high degree of similarity between pulse waveforms under different prestressing pressures. The stability of the extracted pulse wave contours and typical characteristic parameters under various prestressing pressures mean that the KIP sensor can assist precision medicine and provide clinical decision support for personalized healthcare.

To demonstrate the accuracy of the KIP sensor for continuous pulse wave monitoring, a commercial medical instrument (BLT-M8000) and the designed KIP sensor-based wireless cardiovascular monitoring system were simultaneously utilized to measure pulse waves, as illustrated in **Figure 5**a. After being in a completely relaxed state for 5–10 min, participants were asked to stay seated for 3 min for the test. Two identical encapsulated commercial blood pressure probes were worn on the left and right index fingers of a 53-year-old participant, as shown in Figure 5b and Movie S3, Supporting Information, where the photoelectric sensor and the KIP sensor were tested under the same pressure by adjusting probe positioning. The two resulting fingertip pulse waves were consistent in characteristic points under applied external pressure, indicating that the KIP sensor can measure the fingertip pulse waveform accurately as a commercial instrument. Furthermore, to verify the stability of the measured physiological signal for long-term health monitoring, radial artery pulse waveforms were acquired at the same time daily for eight consecutive weeks (Figure 5c). The pulse waveform remained highly similar with all the characteristic points accurately identified, which indicates that the KIP sensor holds decent mechanical robustness and reliability for practical long-term applications.

To demonstrate that the KIP sensor can be widely applicable to different individuals, the radial pulse waves were measured from different subjects. Tests were carried out between seven and nine o'clock in the morning at a room temperature of 23 °C and involved a total of 45 participants, 15 from each group: the healthy group, ages 21–75 years old, the hypertension (HTN) group, ages 30–73 years old, and the coronary heart disease (CHD) group, ages 47–78 years old. Figure S14a–c, Supporting Information show the recorded real-time pulse waves over several pulse periods for three participants, with each containing three important feature points characteristic of pulse waves: the peak of the advancing wave (P_s), the peak of the reflected wave (P_i), and the peak of the dicrotic wave (P_d).[57] These characteristic points can provide diagnostic references about the cardiovascular system, such as arterial elasticity, peripheral resistance, and left ventricular contractility. Even under a large

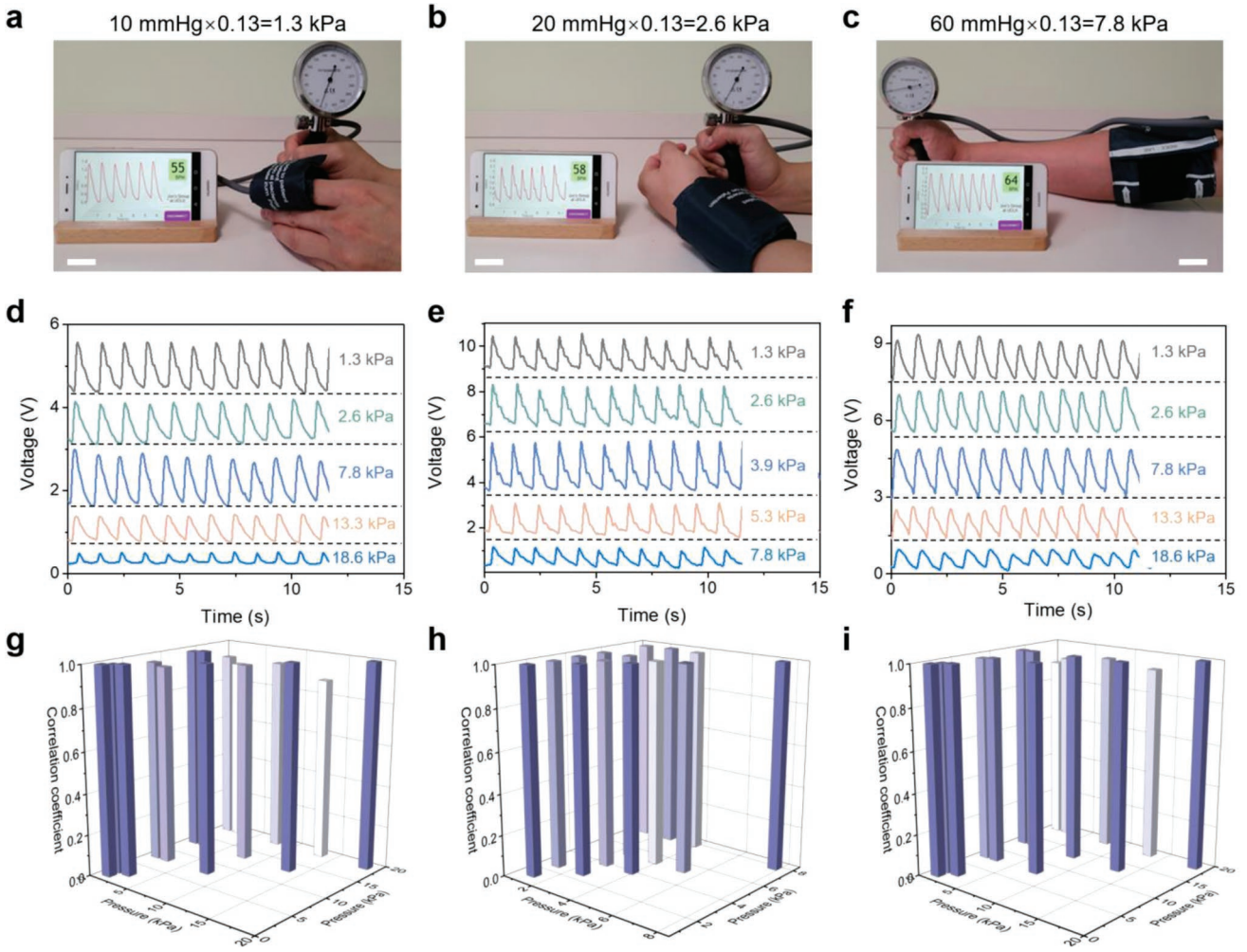

Figure 4. Performance of the KIP sensor. a–c) Photographs showing that the wireless cardiovascular monitoring system is worn on the human fingertip (a), the radial artery (b), and the brachial artery (c) for pulse wave measurement under different prestressing pressure (Scale bar: 2 cm). d–f) The measured pulse waveforms from the three places under different prestressing pressures. g–i) Analysis of the correlation coefficients between different waveforms from the three places.

prestressing pressure, the KIP sensor's high sensitivity and stability allow it to differentiate between these three distinct peaks. It can be observed that the KIP sensor successfully captures the characteristic points. However, it is worthy to note that they are less prominent for the elderly, especially for point P_i, which can be attributed to the pulse waves spreading through the arteries at a higher velocity. Furthermore, the frequency spectra of the three participants are significantly different (Figure S14d–f, Supporting Information). In the low-frequency range, the four strong periodic lines are higher in the younger subjects than in the older ones. Similarly, in the high-frequency range, the periodic line patterns in the older subjects are much weaker than in the younger subjects.

Additionally, the reflected wave arrives back to the aorta before the late systole when there is a decrease in vascular elasticity that is commonly seen in the elderly. Based on the acquired pulse waveforms, two of the most widely used hemodynamic parameters were quantified: the augmentation index $AI_r = P_i/(P_s - P_d)$, and the time delay between the P_s and P_i $\Delta T_{DVP} = T_{Pi} - T_{Ps}$,[58,59] which are calculated for different participants. For the HTN and CHD groups, the AI_r values were higher than those of the healthy group. On the other hand, the ΔT_{DVP} values of the HTN and CHD groups were lower than those in the healthy group. To verify the applicability of KIP sensor in different people, we measured 45 participants' pulse waveforms and compared their two parameters, AI_r and ΔT_{DVP}, as presented in Figure S15, Supporting Information and Table S1, Supporting Information. It can be found that the AI_r values of the HTN and CHD groups were all increased compared with that of the healthy group and have statistical difference ($P_{HTN} < 0.01$, $P_{CHD} < 0.001$). Meanwhile, the ΔT_{DVP} values of the HTN and CHD groups were all reduced compared with the healthy group and have statistical difference ($P_{HTN} \ll 0.001$, $P_{CHD} \ll 0.001$). These noticeable differences successfully verify the capability of our KIP sensor to distinguish the subtle differences between various pulse waveforms, which may provide an efficient alternative for real-time assessing cardiovascular health status in addition to the current expensive and bulky medical commercial equipment in the hospital.

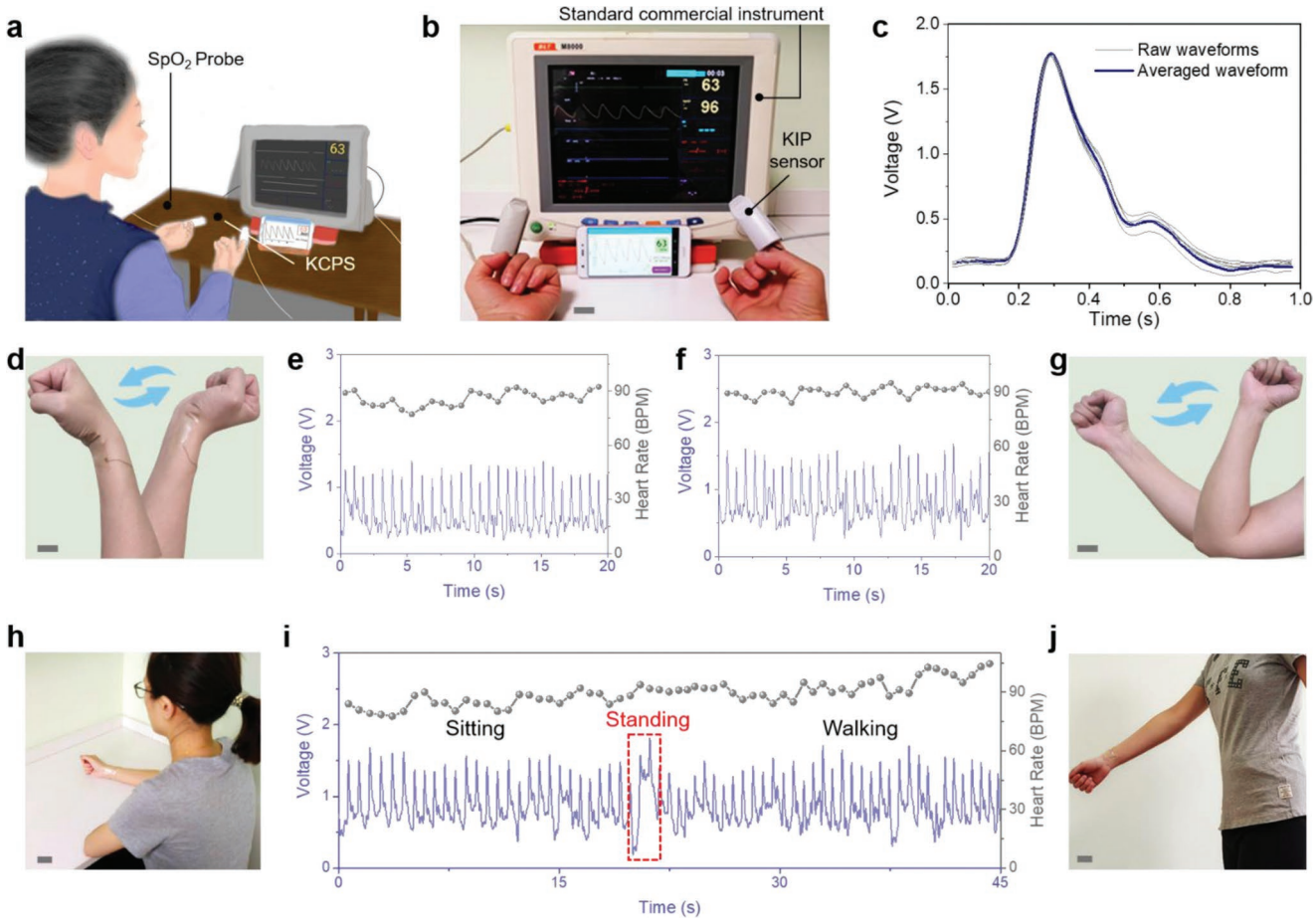

Figure 5. Motion artifact sensing with the KIP sensor-based wireless cardiovascular monitoring system. a) Schematic of fingertip pulse wave monitoring validation using the KIP sensor and standard medical device simultaneously. b) The photoelectric sensor and the KIP sensor were tested under the same prestressing force for real-time fingertip pulse monitoring using the wireless cardiovascular monitoring system (Scale bar: 2 cm). c) Device robustness was demonstrated after 8 weeks of continuous pulse measurement. d,g) The device was attached to the wrist to perform dynamic health monitoring under rotation (d) and arm swing (g) in a wearable manner (Scale bars: 2 cm). e,f) The measured pulse waveforms from the two motion artifacts. h–j) Photograph and the real-time artery pulse signal measured by KIP sensor during sitting and walking (Scale bars: 2 cm).

2.5. Pulse Monitoring with Motion Artifacts

Despite significant advances in wearable health monitoring devices, there is no study that involves a mobile wearable pressure sensor that can detailedly capture such weak pulse signals during daily activities because of their conformability and vulnerability to motion artifacts. Motion artifacts are especially problematic in the wearable health monitoring system and can lead to misinterpretation and misdiagnosis. Studies have demonstrated that misdiagnosis due to motion artifacts caused by inappropriate adhesion of sensors or electrodes to human skin during body movement can significantly reduce patients' quality of life. To validate the response of our device to induced motions, two experiments were carried out, including wrist rotation and arm swing while recording the radial pulse signal, as shown in Figure 5d,g (Movie S4, Supporting Information). And the corresponding pulse waveforms are shown in Figure 5e,f. The measurement results demonstrate that although the bending of human body parts causes a large physical disturbance, the KIP sensor is sensitive to expressing each cardiac cycle using electrical signals with characteristic peak points. We measured the radial pulse signal of a 29-year-old pregnant woman during arm swing under prestressing pressure of 3.9 kPa, as shown in Figure S16, Supporting Information. From the acquired signals, it can be found that the wave shape with characteristic points can be successfully captured during arm swing by our KIP sensor. This indicates that the proposed device can be successfully applied in pulse measurement with prestressing pressure under motion artifacts.

Meanwhile, we also studied the fingertip signals with motion artifacts, we gave a side-by-side comparisons of fingertip monitoring. Here, two experiments were carried out, including fingertip bending back and forth, and walking while recording the fingertip pulse signal. When the device is attached on the curved joints of fingertips, the highly conformal and sensitive KIP sensor can precisely detect the pulse wave signals when the fingertip bending back and forth at a constant rotate speed (65 ± 1.4 rad s^{-1}) (Figure S17a, Supporting Information). The real-time cardiovascular data of measured fingertip pulse wave is demonstrated in Figure S17b, Supporting Information. Furthermore, we also measured the fingertip pulse signal during arm swing. The acquired pulse wave signal is shown in

Figure S18, Supporting Information. Compared with the quiescent condition, the peak points of the pulse waveform will be a slight fluctuation with motion artifacts. However, it is worth noting that no matter what motion artifacts are, the KIP sensor can accurately extract the peak point of the pulse wave, which provides a good guarantee for the accuracy of calculating the heart rate. These results are attributed to the high conformality and excellent sensitivity, which enable our KIP sensor respond to weak fingertip pulse signals with motion artifacts. In addition, walking is considered to be one of the most iconic daily activities. A participant was instructed to remain in a stable sitting position for 16 s and then walk for 16 s to perform a simple dynamic pulse test (Figure 5h–j). A noticeable increase in heart rate (HR) could be observed as the participant sat and kept a calm meditative mood, but then it rose as the participant walked. The detection of the change in HR indicates that the proposed KIP senor is compliant with cardiac diagnostics. The pulse signals and heart rate can return to a steady state promptly after significant motion artifacts interference.

3. Conclusion

We developed a KIP sensor for wearable monitoring of subtle physiological signals. The unique structural design of the pressure sensor allows for it to reach an excellent sensitivity of 35.2 mV Pa^{-1} with a high mechanical durability (>84 000 operation cycles). Due to the enhancement in conformability and improvement in sensitivity, the KIP sensor can accurately capture the pulse wave signals from different body artery sites under a wide range of prestressing pressures (1.3–18.6 kPa), even with heavy motion artifacts. In addition, an wireless cardiovascular monitoring system was further developed to conveniently display the measured cardiovascular parameters via a cellphone APP, capable of providing measurement results as precise as that of commercial medical instruments. This work renders a reliable and user-friendly approach for pulse wave measurement and cardiovascular health condition evaluation with a collection of compelling features, including flexibility, light weight, and high sensitivity. We anticipate that the wearable KIP sensor can be adopted for personalized cardiovascular healthcare.

4. Experimental Section

Fabrication of Kirigami Structure and Nanowires Array on PTFE Surface: A PTFE film with 25 µm thickness was cleaned by menthol, isopropyl alcohol, and deionized water. A reactive-ion etching (RIE) system was then used to fabricate the aligned nanowires on the PTFE surface. O_2 gases were injected into the RIE chamber with flow ratios of 30.0 sccm. 100 W was used to accelerate as the power source of the plasma ions. The nPTFE were obtained after about 10–15 min reaction time. Finally, the nPTFE with kirigami structure was made using a high-precision laser cutting device.

Fabrication of a KIP Sensor: PTFE and PET were chosen as the triboelectric layers for device fabrication. A layer of ITO was deposited onto the PET thin film (75 µm) with the ITO acting as the electrode. Furthermore, 50 µm-thick optical clear adhesive was attached on the four corners of the PET thin film, and then pasted on the kirigami constructed nPTFE layer.

Experimental Setup for Pressure and Electrical Characterization: The SEM images of the nanowire-patterned PTFE were characterized by a JEOL JSM-7800F. A well-defined sinusoidal period load was provided by a function generator (Stanford DS345) and an amplifier (LabworkPa-13). The electrometer (Keithley 6514) was employed to capture and record the open-circuit voltage and short-circuit current of the MMTPS. The external pressure was measured by a dual-range force Gauge (DSM-2).

Statistical Analysis: The *t*-test was used to compare mean values in groups of samples for cardiovascular health status assessment. Error bars were calculated using mean ± SD (standard deviation) with each group size $n = 15$. The reported *p*-values were calculated for groups with unequal variance using the Origin software and a two-sample *t*-test. Reported *p*-values for all experiments corresponded to $*p < 0.05$, $**p < 0.01$, and $***p < 0.001$.

Human Subject Study: The KIP sensor used for wearable cardiovascular monitoring was performed using human subjects in compliance with all the ethical regulations under a protocol (ID: 20–001882) that was approved by the Institutional Review Board at University of California, Los Angeles. All participating subjects belonged to University of California, Los Angeles and provided informed consent before participation in the study.

Supporting Information

Supporting Information is available from the Wiley Online Library or from the author.

Acknowledgements

K.M. and X.X. contributed equally to this work. J.C. acknowledges the Henry Samueli School of Engineering and Applied Science and the Department of Bioengineering at the University of California, Los Angeles for the startup support, the 2021 Hellman Follow Grant, the UCLA Pandemic Resources Program Research Award, and the Research Recovery Grant by the UCLA Academic Senate. J.Y. and W.D. acknowledges the National Natural Science Foundation of China (NSFC 52175281, NSFC 62104125), and Youth Innovation Promotion Association of Chinese Academy of Sciences (2021382). K.M. acknowledges the Excellent Team Project for Technological Innovation and Enterpreneurship of Jilin Province (Grant No.20210509051RQ).

Conflict of Interest

The authors declare no conflict of interest.

Data Availability Statement

The data that support the findings of this study are available from the corresponding author upon reasonable request.

Keywords

biomonitoring, kirigami, motion artifacts, triboelectric nanogenerators, wearable bioelectronics

Received: March 17, 2022
Revised: May 29, 2022
Published online:

[1] K. Meng, X. Xiao, W. Wei, G. Chen, A. Nashalian, S. Shen, X. Xiao, J. Chen, *Adv. Mater.* **2022**, *34*, 2109357.
[2] S. Shen, X. Xiao, X. Xiao, J. Chen, *Chem. Commun.* **2021**, *57*, 5871.
[3] N. Ghasemzadeh, A. M. Zafari, *Cardiol. Res. Pract.* **2011**, *2011*, 164832.
[4] M. D. Stern, *Nature* **1975**, *254*, 56.
[5] R. Kelly, C. Hayward, A. Avolio, M. O'rourke, *Circulation* **1989**, *80*, 1652.
[6] C. D. Leake, *Circulation* **1962**, *1*, 11.
[7] P. C. Hsu, H. T. Wu, C. K. Sun, *J. Med. Syst.* **2018**, *42*, 43.
[8] B. E. Westerhof, I. Guelen, N. Westerhof, J. M. Karemaker, A. Avolio, *Hypertension* **2006**, *48*, 595.
[9] G. Chen, X. Xiao, X. Zhao, M. Bick, T. Tat, J. Chen, *Chem. Rev.* **2022**, *122*, 3259.
[10] M. A. P. Mahmud, T. Tat, X. Xiao, P. Adhikary, J. Chen, *Exploration* **2021**, *1*, 20210033.
[11] G. Schwartz, B. C. Tee, J. Mei, A. L. Appleton, D. H. Kim, H. Wang, Z. Bao, *Nat. Commun.* **2013**, *4*, 1859.
[12] X. Zeng, Y. Hu, *ACS Nano* **2021**, *15*, 9238.
[13] C. Pang, J. H. Koo, A. Nguyen, J. M. Caves, M. G. Kim, A. Chortos, K. Kim, P. J. Wang, J. B. Tok, Z. Bao, *Adv. Mater.* **2015**, *27*, 634.
[14] A. Libanori, G. Chen, X. Zhao, Y. Zhou, J. Chen, *Nat. Electron.* **2022**, *5*, 142.
[15] Q. Lin, J. Huang, J. Yang, Y. Huang, Y. Zhang, Y. Wang, J. Zhang, Y. Wang, L. Yuan, M. Cai, X. Hou, W. Zhang, Y. Zhou, S. G. Chen, C. F. Guo, *Adv. Healthcare Mater.* **2020**, *9*, 2001023.
[16] C. L. Choong, M. B. Shim, B. S. Lee, S. Jeon, D. S. Ko, T. H. Kang, J. Bae, S. H. Lee, K. E. Byun, J. Im, Y. J. Jeong, C. E. Park, J. J. Park, U. I. Chung, *Adv. Mater.* **2014**, *26*, 3451.
[17] X. Zeng, Y. Liu, F. Liu, W. Wang, X. Liu, X. Wei, Y. Hu, *Nano Energy* **2022**, *92*, 106777.
[18] Y. Si, X. Wang, C. Yan, L. Yang, J. Yu, B. Ding, *Adv. Mater.* **2016**, *28*, 9512.
[19] Q. Wei, G. Chen, H. Pan, Z. Ye, C. Au, C. Chen, X. Zhao, Y. Zhou, X. Xiao, H. Tai, Y. Jiang, G. Xie, Y. Su, J. Chen, *Small Methods* **2021**, *6*, 2101051.
[20] Y. Su, C. Chen, H. Pan, Y. Yang, G. Chen, X. Zhao, W. Li, Q. Gong, G. Xie, Y. Zhou, S. Zhang, H. Tai, Y. Jiang, J. Chen, *Adv. Funct. Mater.* **2021**, *31*, 2010962.
[21] Y. Su, W. Li, L. Yuan, C. Chen, H. Pan, G. Xie, G. Conta, S. Ferrier, X. Zhao, G. Chen, H. Tai, Y. Jiang, J. Chen, *Nano Energy* **2021**, *89*, 106321.
[22] X. Xiao, J. Yin, G. Chen, S. Shen, A. Nashalian, J. Chen, *Matter* **2022**, *5*, 1342.
[23] W. Fan, Q. He, K. Meng, X. Tan, Z. Zhou, G. Zhang, J. Yang, Z. L. Wang, *Sci. Adv.* **2020**, *6*, eaay2840.
[24] S. Zhang, M. Bick, X. Xiao, G. Chen, A. Nashalian, J. Chen, *Matter* **2021**, *4*, 845.
[25] L. Jin, X. Xiao, W. Deng, A. Nashalian, D. He, V. Raveendran, C. Yan, H. Su, X. Chu, T. Yang, W. Li, W. Yang, J. Chen, *Nano Lett.* **2021**, *20*, 6404.
[26] S. Shen, X. Xiao, X. Xiao, J. Chen, *ACS Appl. Energy Mater.* **2021**, *5*, 3952.
[27] X. Xiao, G. Chen, A. Libanori, J. Chen, *Trend. Chem.* **2021**, *3*, 279.
[28] Y. Zhou, X. Zhao, J. Xu, Y. Fang, G. Chen, Y. Song, S. Li, J. Chen, *Nat. Mater.* **2021**, *20*, 1670.
[29] G. Chen, X. Zhao, S. Andalib, J. Xu, Y. Zhou, T. Tat, K. Lin, J. Chen, *Matter* **2021**, *4*, 3725.
[30] X. Zhao, Y. Zhou, J. Xu, G. Chen, Y. Fang, T. Tat, X. Xiao, Y. Song, S. Li, J. Chen, *Nat. Commun.* **2021**, *12*, 6852.
[31] A. A. Kamshilin, I. S. Sidorov, L. Babayan, M. A. Volynsky, R. Giniatullin, O. V. Mamontov, *Biomed. Opt. Express* **2016**, *7*, 5138.
[32] S. Rajala, H. Lindholm, T. Taipalus, *Physiol. Meas.* **2018**, *39*, 075010.
[33] D. Castaneda, A. Esparza, M. Ghamari, C. Soltanpur, H. Nazeran, *Int. J. Biosens. Bioelectron.* **2018**, *4*, 195.
[34] M. Elgendi, *Curr. Cardiol. Rev.* **2012**, *8*, 14.
[35] A. G. Miller, A. J. Bardin, *Respir. Care.* **2016**, *61*, 383.
[36] C. Wang, X. Li, H. Hu, L. Zhang, Z. Huang, M. Lin, Z. Zhang, Z. Yin, B. Huang, H. Gong, S. Bhaskaran, Y. Gu, M. Makihata, Y. Guo, Y. Lei, Y. Chen, C. Wang, Y. Li, T. Zhang, Z. Chen, A. P. Pisano, L. Zhang, Q. Zhou, S. Xu, *Nat. Biomed. Eng.* **2018**, *2*, 687.
[37] C. Wang, B. Qi, M. Lin, Z. Zhang, M. Makihata, B. Liu, S. Zhou, Y.-h. Huang, H. Hu, Y. Gu, Y. Chen, Y. Lei, T. Lee, S. Chien, K.-I. Jang, E. B. Kistler, S. Xu, *Nat. Biomed. Eng.* **2021**, *5*, 749.
[38] Y. Fang, X. Zhao, T. Tat, X. Xiao, G. Chen, J. Xu, J. Chen, *Matter* **2021**, *4*, 1102.
[39] Y. Fang, Y. Zou, J. Xu, G. Chen, Y. Zhou, W. Deng, X. Zhao, M. Roustaei, T. K. Hsiai, J. Chen, *Adv. Mater.* **2021**, *33*, 2104178.
[40] G. Chen, C. Au, J. Chen, *Trend. Biotechnol.* **2021**, *39*, 1078.
[41] T. Tat, A. Libanori, C. Au, A. Yau, J. Chen, *Biosens. Bioelectron.* **2021**, *171*, 112714.
[42] J. Lama, A. Yau, G. Chen, A. Sivakumar, J. Chen, *J. Mater. Chem. A* **2021**, *9*, 19149.
[43] X. Xiao, Y. Fang, X. Xiao, J. Xu, J. Chen, *ACS Nano* **2021**, *15*, 18633.
[44] Z. Zhang, Z. Pi, B. Liu, *IEEE. Trans. Biomed. Eng.* **2015**, *62*, 522.
[45] M. K. Blees, A. W. Barnard, P. A. Rose, S. P. Roberts, K. L. McGill, P. Y. Huang, A. R. Ruyack, J. W. Kevek, B. Kobrin, D. A. Muller, P. L. McEuen, *Nature* **2015**, *524*, 204.
[46] A. S. Gladman, E. A. Matsumoto, R. G. Nuzzo, L. Mahadevan, J. A. Lewis, *Nat. Mater.* **2016**, *15*, 413.
[47] K. Xu, Y. Lu, S. Honda, T. Arie, S. Akita, K. Takei, *J. Mater. Chem. C* **2019**, *7*, 9609.
[48] K. Yong, S. De, E. Y. Hsieh, J. Leem, N. R. Aluru, S. Nam, *Mater. Today* **2020**, *34*, 58.
[49] H. C. Lee, E. Y. Hsieh, K. Yong, S. Nam, *Nano Res.* **2020**, *13*, 1406.
[50] B. Gao, A. Elbaz, Z. He, Z. Xie, H. Xu, S. Liu, E. Su, H. Liu, Z. Gu, *Adv. Mater. Technol.* **2018**, *3*, 1700308.
[51] K. Meng, S. Zhao, Y. Zhou, Y. Wu, S. Zhang, Q. He, X. Wang, Z. Zhou, W. Fan, X. Tan, J. Yang, J. Chen, *Matter* **2020**, *2*, 896.
[52] X. Xiao, X. Xiao, A. Nashalian, A. Libanori, Y. Fang, X. Li, J. Chen, *Adv. Healthcare Mater.* **2021**, *10*, 2100975.
[53] Z. Zhao, C. Yan, Z. Liu, X. Fu, L. M. Peng, Y. Hu, Z. Zheng, *Adv. Mater.* **2016**, *28*, 10267.
[54] Z. Zhou, K. Chen, X. Li, S. Zhang, Y. Wu, Y. Zhou, K. Meng, C. Sun, Q. He, W. Fan, E. Fan, Z. Lin, X. Tan, W. Deng, J. Yang, J. Chen, *Nat. Electron.* **2020**, *3*, 571.
[55] X. Xiao, X. Xiao, Y. Zhou, X. Zhao, G. Chen, Z. Liu, Z. Wang, C. Lu, M. Hu, A. Nashalian, S. Shen, K. Xie, W. Yang, Y. Gong, W. Ding, P. Servati, C. Han, S. Dou, W. Li, *J. Chen. Sci. Adv.* **2021**, *7*, eabl3742.
[56] J. He, P. Xiao, W. Lu, J. Shi, L. Zhang, Y. Liang, C. Pan, S.-W. Kuo, T. Chen, *Nano Energy* **2019**, *59*, 422.
[57] A. P. Avolio, M. Butlin, A. Walsh, *Physiol. Meas.* **2010**, *31*, R1.
[58] W. W. Nichols, *Am. J. Hypertens.* **2005**, *18*, 3.
[59] K. Kohara, Y. Tabara, A. Oshiumi, Y. Miyawaki, T. Kobayashi, T. Miki, *Am. J. Hypertens.* **2005**, *18*, 11.